

## Influence of structural, electronic and optical properties of boron and nitrogen doping in tetragonal $\text{PbTiO}_3$ : insight from first-principles

T. Y. Lu, B. R. Huang, Z. Q. Wen<sup>\*</sup>, L. T. Huang, X. P. Wei, Z. G. Zou

*Key Laboratory of New Processing Technology for Nonferrous Metals and Materials, Ministry of Education, School of Materials Science and Engineering, Guilin University of Technology, Guilin 541004, China*

The structural, electronic and optical properties of intrinsic, B- and N-doped tetragonal  $\text{PbTiO}_3$  are investigated by first-principles calculations. After doping with B (N) atom, the stability of the system decreases, but it is still thermodynamically stable. B-doped (N-doped)  $\text{PbTiO}_3$  appear new B-2p (N-2p) impurity bands near Fermi level, reducing the bandwidth from 2.02eV to 0.56eV (0.43eV). Imaginary part of dielectric function has the largest peak at the photon energy of 5.81 eV, which originates from the transition of electrons from the occupied O-2p VB states to the unoccupied Ti-3d CB states. The static refractive index of B- and N-doped  $\text{PbTiO}_3$  are larger than that of  $\text{PbTiO}_3$ . B-doped (N-doped)  $\text{PbTiO}_3$  can increase the light absorption capacity of near-infrared wavelengths and visible light, and energy loss in the visible light range is very small, indicating that B- and N-doping are expected to improve the optical properties of  $\text{PbTiO}_3$ .

(Received March 9, 2022; Accepted July 1, 2022)

*Keywords:* First-principles,  $\text{PbTiO}_3$ , Doping, Optical properties

### 1. Introduction

Lead titanate ( $\text{PbTiO}_3$ ) is an  $\text{ABO}_3$ -type perovskite oxide materials. It has aroused great research interest due to large dielectric constant, noticeable ferroelectric, piezoelectric and pyroelectric effect [1, 2]. Hence,  $\text{PbTiO}_3$  is widely used in many fields, such as filters, high-capacity computer memory cells and infrared sensor [3-8].

$\text{PbTiO}_3$  exhibits tetragonal symmetry ( $P4mm$ ) at room temperature, and it is transformed into cubic state ( $Pm-3m$ ) above 763K (Curie temperature) [9, 10]. Significantly, it is very difficult to successfully fire traditional  $\text{PbTiO}_3$  ceramics. When the sintering temperature is cooled to the Curie temperature, microcracks are prone to appear, but adding some dopants can inhibit the cracking. During preparation and annealing of  $\text{PbTiO}_3$ , doping with new elements can change the interaction between the microstructure and protons to tune the performance [11]. Some predecessors doped  $\text{PbTiO}_3$  with different concentrations and elements and obtained ceramics with better ferroelectric stability [12-15]. Stashans *et al.* [16] studied the electronic structure of Zr-doped  $\text{PbTiO}_3$  using first-principles, and found that Zr-doped  $\text{PbTiO}_3$  could improve the

---

\* Corresponding author: wenzhiqin@glut.edu.cn

ferroelectric properties. Wu *et al.* [17] used  $\text{PbTiO}_3$  series ( $\text{BiScO}_3\text{-PbTiO}_3$ ) ceramics to make piezoelectric bimorph type harvesters, which have excellent vibration energy harvesting performance at high temperatures.

Tetragonal  $\text{PbTiO}_3$  has a bandwidth of 3.0~4.5 eV [18-20], only the ultra violet (UV) part of sunlight (4% of solar energy) [21] can be used, and it is difficult to exert its own optical properties more effectively. Fortunately, we can improve the absorption efficiency of  $\text{PbTiO}_3$  by doping some elements. Oanh *et al.* [22] prepared Mn-doped  $\text{PbTiO}_3$  by the sol-gel method, which can effectively absorb sunlight and separate carriers through the bulk photovoltaic effect of ferroelectric materials. Abirami *et al.* [23] prepared intrinsic  $\text{PbTiO}_3$  and Ag-doped  $\text{PbTiO}_3$  nanoparticles by hydrothermal synthesis, Ag (0.03%) doped  $\text{PbTiO}_3$  nanoparticles showed excellent photocatalytic activity and high repetitive use. Lemziouka *et al.* [24] prepared Cu-doped  $\text{PbTiO}_3$  by sol-gel method, which reduced the transition temperature and enhanced the light absorption coefficient. Recently, almost all the elements doped with  $\text{PbTiO}_3$  are metal elements, but there are few reports on the research of doping  $\text{PbTiO}_3$  with non-metal elements. Non-metal doped  $\text{PbTiO}_3$  such as N doping causes widespread concern by first-principles. Niu *et al.* [1, 25] studied N-doped cubic  $\text{PbTiO}_3$  using first-principles method, it found that N-doped  $\text{PbTiO}_3$  system showed p-type conductivity. To date, other non-metal such as B element doping have not been reported, and the effect of B and N atom doping on the stability, electronic structure and optical properties of tetragonal  $\text{PbTiO}_3$  is still unclear.

In this paper, we study structural, electronic and optical properties of intrinsic tetragonal, B- and N-doped tetragonal  $\text{PbTiO}_3$  based on first-principles calculations. Besides, we compare optical properties of intrinsic, B- and N-doped tetragonal  $\text{PbTiO}_3$  in the range of visible light energy, aiming to investigate the absorption efficiency in visible light.

## 2. Computational details

All the first-principles calculations for tetragonal, B- and N-doped  $\text{PbTiO}_3$  are based on density functional theory (DFT) with spin polarization, which is performed by Cambridge Serial Total Energy Package (CASTEP) [26, 27] in Materials Studio (MS). The plane wave ultra-soft pseudopotential method [28] along with Perdew-Burke-Ernzerhof (PBE) version of the generalized gradient approximation (GGA) [29] have been used to represent exchange-correlation functional. In our calculations, the energy cutoff ( $E_{cut}$ ) is set as 500 eV, and a  $6\times 6\times 6$  k-point Monkhorst-Pack mesh is used for the first Brillouin zone. The self-consistent field (SCF) convergence threshold is  $1\times 10^{-6}$  eV/atom, the convergence condition is that the energy change of each atom is within  $1\times 10^{-5}$  eV, the maximum force of the atom is smaller than 0.03eV/Å, the maximum pressure is smaller than 0.05GPa, and the maximum displacement is smaller than 0.001 Å. After convergence testing, all parameters are guaranteed to converge. The valence electron configuration involved in the calculation are  $5d^{10}6s^2 6p^2$  for Pb,  $3s^2 3p^6 3d^2 4s^2$  for Ti,  $2s^2 2p^4$  for O,  $2s^2 2p^1$  for B and  $2s^2 2p^3$  for N.

In order to simulate the doping systems, we use  $2\times 2\times 2$  tetragonal  $\text{PbTiO}_3$  supercell containing 40 atoms as the calculation model, as shown in Fig. 1. As we know, there are two different kinds of O atoms in tetragonal  $\text{PbTiO}_3$ , labeled  $\text{O}_1$  and  $\text{O}_2$ , respectively. After testing, the energy of the system doped with B or N atom at  $\text{O}_1$  position is lower than that of  $\text{O}_2$

position. Therefore, B or N atom are selected to replace an O atom at the position of O<sub>1</sub>. The simulated doping concentration is 2.5at%.

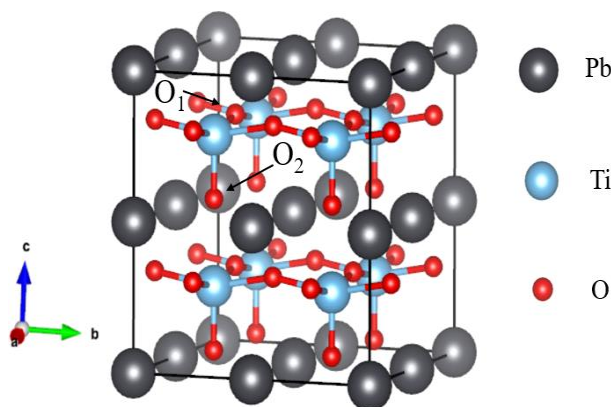


Fig. 1. Schematic of  $2 \times 2 \times 2$  supercell crystal structure of tetragonal  $\text{PbTiO}_3$

### 3. Results and discussion

#### 3.1. optimize structure

The calculated lattice constants and formation enthalpy of intrinsic, B- and N-doped tetragonal  $\text{PbTiO}_3$  are tabulated in Table 1. Compared with the experimental value [30], the  $a$ -axis is underestimated by 1.1%, and the  $c$ -axis is overestimated by 15.6%. But the value of the optimized volume is almost the same as reported by Wang [31] and Zhang [32]. Moreover, the calculated formation enthalpy of intrinsic  $\text{PbTiO}_3$  is well in agreement with Ge's report [11], which proves that the selected parameters and methods are feasible. The degree of overlap of atomic orbitals between B (N) atom and Ti atom are weakened after doping B (N) atom, which leads to the increase of unit cell volume. Since the relative atomic radius of B and N atom (0.82 and 0.75) is larger than that of O atom (0.74), and the electronegativity of B and N atom (2.04 and 3.04) is smaller than that of O atom (3.44).

Crystal stability is connected to the formation enthalpy. Generally speaking, the formation enthalpy is less than zero, the system is stable [33, 34]. The formation enthalpy  $\Delta H_f$  of the system can be calculated using equation (1):

$$\Delta H_f(\text{PbTiO}_{(24-x)/8}\text{X}_{x/8}) = \frac{1}{8} \left[ \frac{E_{total}(\text{Pb}_8\text{Ti}_8\text{O}_{24-x}\text{X}_x) - 8E_{iso}(\text{Pb}) - 8E_{iso}(\text{Ti})}{-(24-x)E_{iso}(\text{O}) - xE_{iso}(\text{X})} \right] \quad (1)$$

where  $X$  is B or N atom,  $x$  is the number of doping atoms,  $E_{total}$  is the total energy of the unit cell,  $E_{iso}$  is the energy of a single atom in the element. The calculated formation enthalpy of intrinsic, B- and N-doped  $\text{PbTiO}_3$  are -12.22 eV, -11.17 eV and -11.65eV, respectively. The formation enthalpy of three systems is negative, and the absolute value of the formation enthalpy of intrinsic  $\text{PbTiO}_3$  is the greatest, which illuminates that the intrinsic  $\text{PbTiO}_3$  is easiest to form.

Table 1. Calculated lattice constants, formation enthalpy and band gaps of intrinsic, B- and N-doped tetragonal  $\text{PbTiO}_3$  along with available experimentally and theoretically data.

	a/ Å	b/ Å	c/ Å	Volume/ Å <sup>3</sup>	$\Delta H_f$ / eV	Band gaps
Intrinsic (Expt.)	3.880[30]	3.880[30]	4.155[30]	62.55[30]	-12.32 [11]	2.08 [31]
Intrinsic (Cal.)	3.846[31]	3.846[31]	4.711[31]	69.68[31]		2.0 [35]
Intrinsic (Cal.)	3.844[32]	3.844[32]	4.766[32]	70.4[32]		2.0 [36]
Intrinsic	3.838	3.838	4.811	70.88	-12.22	2.02
B-doped	3.887	3.788	4.929	72.58	-11.17	0.56
N-doped	3.816	3.839	4.877	71.45	-11.65	0.43

### 3.2. Electron density difference and population analysis

Electron density difference can better display the charge distribution and the bonding properties of the system, electron density difference of intrinsic, B- and N-doped  $\text{PbTiO}_3$  are presented Fig. 2. Blue and red represent the increase and decrease of charge density, respectively. For Fig.2(a), the charge density near Ti atoms is small, while the charge density near  $\text{O}_2$  atoms is large and uniformly distributed in a spherical manner,  $\text{Ti-O}_2$  atoms form strong covalent bonds. The charge density of  $\text{O}_4$  atoms is roughly spherical, but the charge density of  $\text{O}_4$  atoms close to the side of  $\text{Ti}_1$  atoms is higher, and the charge density of  $\text{Ti}_1$  atoms close to the side of  $\text{O}_4$  atoms is lower. The charge density around  $\text{Ti}_1$  atoms is reduced, since the electron is transferred from O-2p states to Ti-3d states, which indicates that  $\text{O}_4$  atoms have strong electronegativity and certain ionic property between  $\text{Ti}_1$  and  $\text{O}_4$  atoms. After doping B atom, the charge density near the B atom tends to close to Ti atoms. Compared with intrinsic  $\text{PbTiO}_3$ , the charge density near Ti atoms decreases more, which emphasizes that the ionic characteristics of Ti-B bonds are stronger than that of Ti-O bonds. After doping N atom, the charge density near the N atom is rule, the electronic cloud between the N atom and Ti atoms overlaps, indicating that the Ti-N bonds is covalent.

The bond population indicates the degree of electron cloud overlap between two bonding atoms [37, 38]. The absolute value of the bond population is close to 1 indicates overlap of the electronic cloud near the bonding atoms is large, and there is strong covalent between bonding atoms. Positive and negative values denote bonding and antibonding respectively. Although the symmetry of the system is reduced after doping, intrinsic  $\text{PbTiO}_3$  has multiple symmetrical bonds, and the change trend of the bonding situation far away from the doping position is roughly the same. Therefore, we only list bond population near the substituted O atom in Table 2. The bond population between  $\text{Ti}_1$ -  $\text{O}_2$  is 0.94, and the bond population between  $\text{Ti}_1$ -  $\text{O}_4$  is 0.73. The overlap degree of the electron cloud between  $\text{Ti}_1$ - $\text{O}_2$  bond is larger, and its covalent characteristic is stronger, this result is consistent with the analysis of charge density differences. After doping with B (N) atom, the bond population between  $\text{Ti}_1$ - $\text{O}_2$  and  $\text{Ti}_2$ - $\text{O}_2$  are reduced from 0.94 to 0.52 (0.51).

The electron cloud orbital overlap is decreased, and the bond length between B-Ti (N-Ti) bonds change from 1.991 to 2.187 (2.028), that's why the volume increases when doping B (N) atom. The bond population between  $Ti_1-O_4$  and  $Ti_2-O_5$  increased from 0.73 to 0.74 (0.75), while the bond population between other Ti-O decreased to varying degrees. Generally speaking, the population of Ti-O bonds are reduced after doping with B (N) atom. In addition, we find that  $Pb_5-O_{13}$  and  $Pb_5-O_{14}$  bonds had shared pairs of electrons in Fig.2 (d), and the charge population also indicates that  $Pb_5-O_{13}$  and  $Pb_5-O_{14}$  bonds has the weak characteristics of covalent bond, so Pb-O bond of intrinsic tetragonal  $PbTiO_3$  is covalent. Our results are consistent with previous reports [39-41].

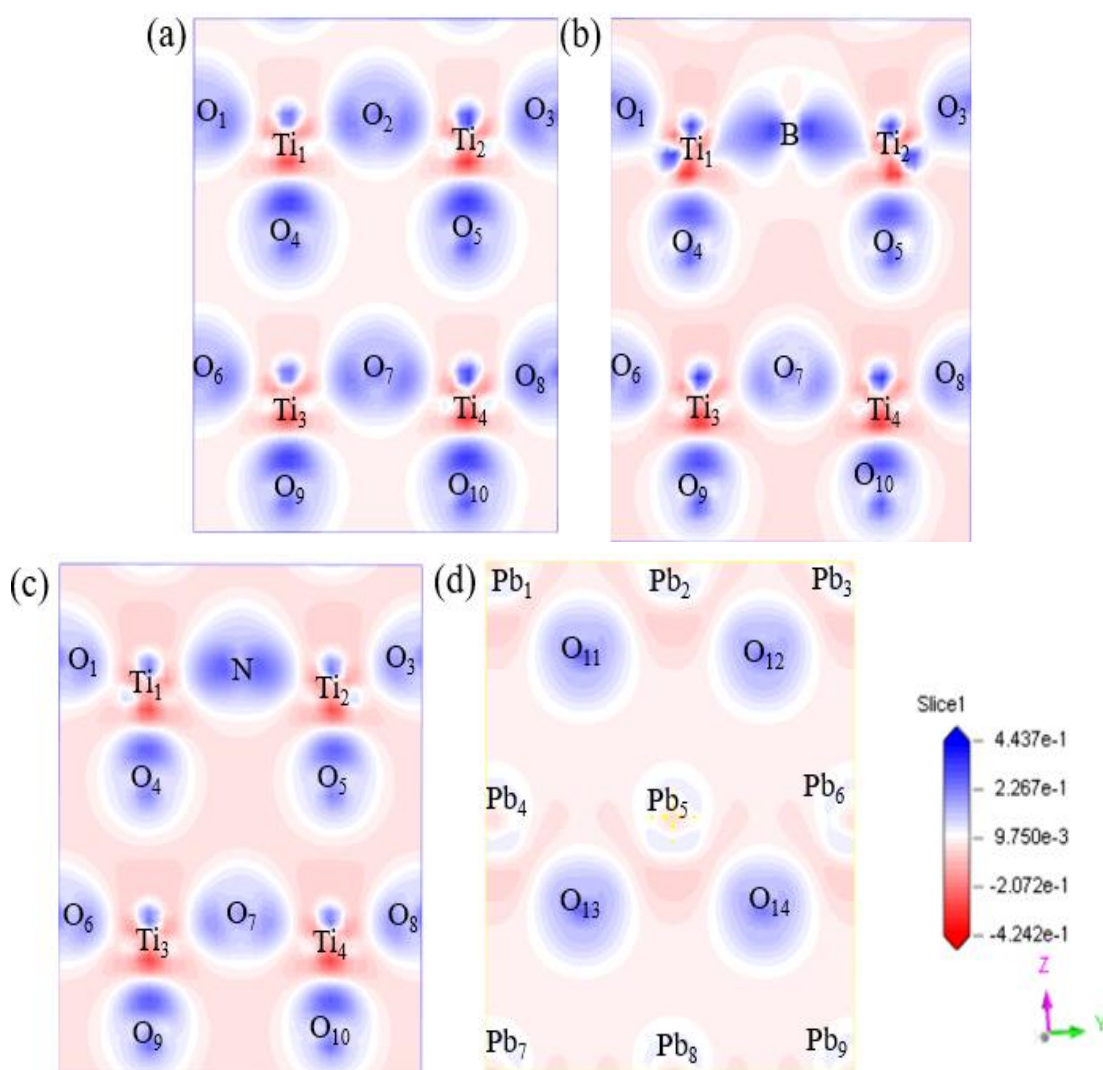


Fig. 2. Calculated electron density difference in the (110) surface of (a) intrinsic, (b) B-doped, (c) N-doping  $PbTiO_3$  and in the (001) surface of (d) intrinsic  $PbTiO_3$ . Colors from blue to red color connotes charge density changes from high to low.

Table 2. The bond length and bond population of intrinsic, B- and N-doped  $\text{PbTiO}_3$ .

Bond	Intrinsic		B-doped		N-doped	
	Bond length/ Å	Bond population	Bond length/ Å	Bond population	Bond length/ Å	Bond population
$\text{O}_1\text{-Ti}_1$	1.991	0.94	1.968	0.36	1.993	0.42
$\text{O}_4\text{-Ti}_1$	1.745	0.73	1.774	0.75	1.758	0.76
$\text{O}_3\text{-Ti}_2$	1.991	0.94	1.969	0.36	1.993	0.42
$\text{O}_5\text{-Ti}_2$	1.745	0.73	1.773	0.75	1.758	0.76
$\text{O}_{11}\text{-Ti}_1$	1.991	0.94	1.975	0.48	1.977	0.45
$\text{O}_{12}\text{-Ti}_2$	1.991	0.94	1.976	0.48	1.977	0.45
$\text{O}_{15}\text{-Ti}_1$	1.991	0.94	1.974	0.48	1.977	0.45
$\text{O}_{16}\text{-Ti}_2$	1.991	0.94	1.974	0.48	1.977	0.45
$\text{O}_{13}\text{-Pb}_5$	2.501	-0.28				
$\text{O}_{14}\text{-Pb}_5$	2.501	-0.28				
$\text{O}_2\text{-Ti}_1$	1.991	0.94				
$\text{O}_2\text{-Ti}_2$	1.991	0.94				
$\text{B-Ti}_1$			2.187	0.52		
$\text{B-Ti}_2$			2.187	0.52		
$\text{N-Ti}_1$					2.028	0.51
$\text{N-Ti}_2$					2.028	0.51

### 3.3. Electronic structure

In order to study the influence of B- and N-doped systems on electronic structure of tetragonal  $\text{PbTiO}_3$ , we calculated band structure and density of states (DOS) of intrinsic and doping systems, as depicted in Fig.3 and Fig.4, respectively. The selection of the high symmetry point of the Brillouin zone is obtained by Ref. [42]. We only analyze the energy bands and DOS near Fermi level because the properties of semiconductors are mainly determined by electrons near Fermi level. The horizontal dotted line represents Fermi level. Valence band maximum (VBM) is located at the  $\Gamma$  point in the Brillouin zone, while conduction band minimum (CBM) is located at the X point, so intrinsic  $\text{PbTiO}_3$  is an indirect bandgap semiconductor. The calculated band gap is 2.020eV, which is basically consistent with the calculation in previous study as showing in Table 1 [31, 35, 36]. However, it is smaller than experimental value of 3.6eV [20], this is because GGA has universal problems with underestimating band gap values [43], but this paper only compares relative relationships between various systems before and after doping, which has no effect on the accuracy of the results. Combined with Fig. 4 (a), it can be seen that CBM of intrinsic  $\text{PbTiO}_3$  is mainly contributed by Ti-3d states, VBM is mainly contributed by O-2p states, in which a small amount of Pb-6s and Ti-3d states are mixed. There is a very flat energy band in the energy range of -7.36 ~ -6.71 eV, which is mainly composed of Pb-6s states. It has strong local characteristics and appears as a sharp peak on DOS spectrum, it elucidates that intrinsic  $\text{PbTiO}_3$  has certain ionic bond characteristics. There is a strong overlap between Ti-3d and O-2p orbitals in the energy range from -4.55 to 0 eV, forming bonding molecular orbitals and showing typical resonance hybridization characteristics, which corresponds to the covalent characteristic of Ti-O bond by electron density

difference analysis. Furthermore, there is also hybridization between Pb-6s states and O-2p states between -1.2~0 eV, leading to a large strain that stabilizes tetragonal PbTiO<sub>3</sub> [36, 40].

Band structure and DOS of B- and N-doped PbTiO<sub>3</sub> are shown in Fig. 3 (b and c) and Fig. 4 (b and c), respectively. The band gap of B- and N-doped PbTiO<sub>3</sub> are 0.56eV and 0.43eV, respectively. Compared with intrinsic PbTiO<sub>3</sub>, the width of band gap is significantly reduced due to the presence of new impurity levels, and the band is denser. For B-doped, both VBM and CBM are located at the U point of the Brillouin zone, expounding that B-doped PbTiO<sub>3</sub> is direct bandgap semiconductor. Several new impurity bands composed of B-2p orbitals are discovered between energy range of 0.23-0.61eV. For N-doped, VBM is located at the  $\Gamma$  point and CBM is located at T point in the Brillouin zone, indicating that N-doped system is indirect bandgap semiconductor. In the energy range of 0.23-0.61eV, there is a spin-up independent band composed of N-2p states, which has a certain bandwidth, implying that it participates in bonding, and N and Ti form covalent bond from Fig.2(c), *i.e.*, both B- and N-doped systems have new impurity states, which makes it easier for electrons in CB to transition to VB.

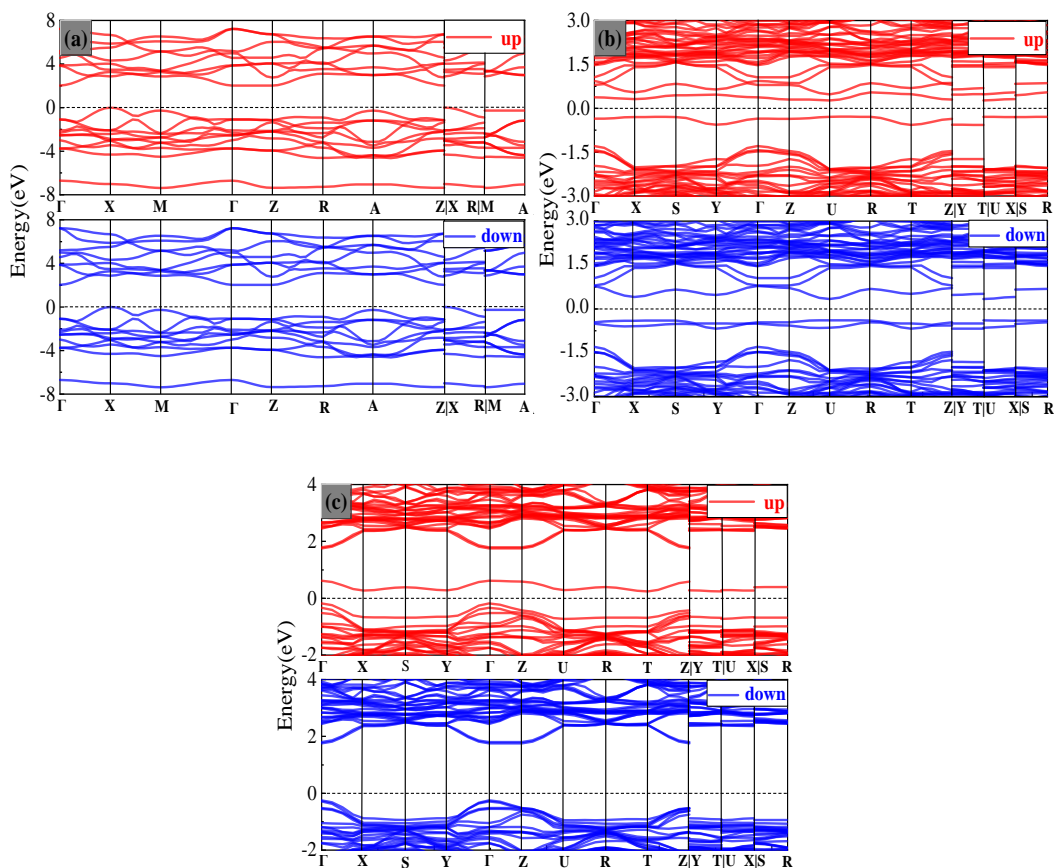


Fig. 3. Calculated band structure of PbTiO<sub>3</sub>: (a) intrinsic, (b) B-doped and (c) N-doped.

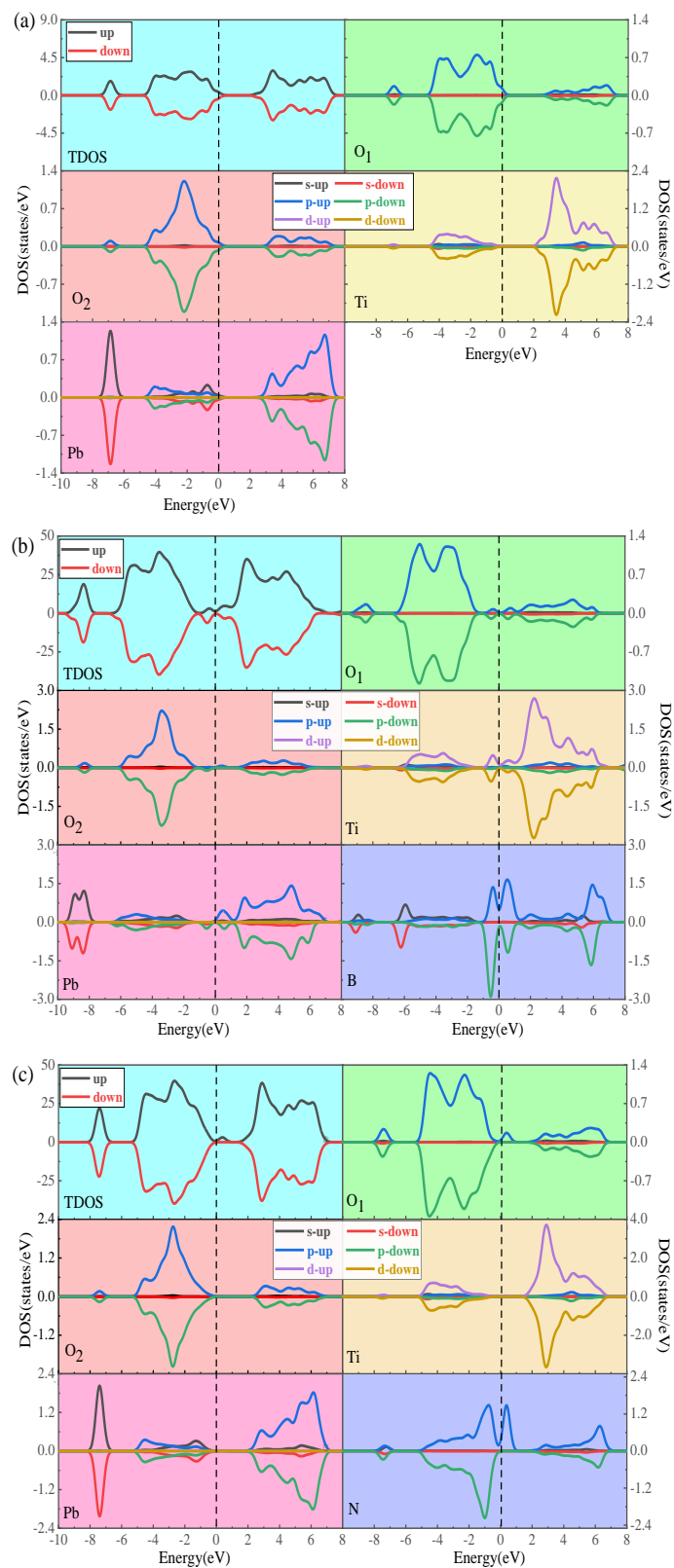


Fig. 4. Total density of states and partial density of states for  $\text{PbTiO}_3$ : (a) intrinsic, (b) B-doped and (c) N-doped.

### 3.4 Optical properties

The optical properties of all solid materials can be expressed in detail with complex dielectric functions. It explains the relationship between band structure and dielectric function, and is a bridge between electronic transition process and solid electronic structure [44], which can be defined by the following equation (2) [45, 46]:

$$\varepsilon(\omega) = \varepsilon_1(\omega) + i\varepsilon_2(\omega) = (n(\omega) + ik(\omega))^2 \quad (2)$$

where  $\varepsilon_1(\omega)$  and  $\varepsilon_2(\omega)$  are real and imaginary parts of complex dielectric function, respectively.  $n(\omega)$  and  $k(\omega)$  are refractive index and extinction coefficient, respectively.  $\omega$  represents the frequency of incident photons.  $\varepsilon_2(\omega)$  can be computed from the momentum matrix elements between occupied and unoccupied wave functions with selection rules, and  $\varepsilon_1(\omega)$  can be obtained from  $\varepsilon_2(\omega)$  through the Kramers-Kronig relationship [47, 48] as shown in equation (3, 4):

$$\varepsilon_2(\omega) = \left( \frac{4\pi^2 e^2}{m^2 \omega^2} \right) \sum_{i,j,k} \langle i | M | j \rangle^2 f_i (1 - f_j) \times \delta(E_{j,k} - E_{i,k} - \omega) d^3k \quad (3)$$

$$\varepsilon_1(\omega) = 1 + \frac{2}{\pi} P \int_0^\infty \frac{\omega' \varepsilon_2(\omega') d\omega'}{(\omega'^2 - \omega^2)} \quad (4)$$

where  $e$  and  $m$  are charge and mass of free electrons,  $M$  denotes the dipole matrix,  $i$  and  $j$  are initial and final states, respectively.  $E_i$  is electron energy of the  $i$ -th state of crystal wave vector  $k$  and  $f_i$  is Fermi distribution function of the  $i$ -th state.  $P$  shows the principal value of integral. The absorption coefficient  $\alpha$ , refractive index  $n$ , extinction coefficient  $k$  and loss function  $L$  can be derived from the dielectric function, which can be expressed by following equation (5-8):

$$\alpha(\omega) = \left[ 2 \left[ \sqrt{\varepsilon_1^2(\omega) + \varepsilon_2^2(\omega)} - \varepsilon_1(\omega) \right] \right]^{\frac{1}{2}} \quad (5)$$

$$n(\omega) = \left[ \frac{\sqrt{\varepsilon_1^2(\omega) + \varepsilon_2^2(\omega)} + \varepsilon_1(\omega)}{2} \right]^{\frac{1}{2}} \quad (6)$$

$$k(\omega) = \left[ \frac{\sqrt{\varepsilon_1^2(\omega) + \varepsilon_2^2(\omega)} - \varepsilon_1(\omega)}{2} \right]^{\frac{1}{2}} \quad (7)$$

$$L(\omega) = -\text{Im} \left( \frac{1}{\varepsilon(\omega)} \right) = \frac{\varepsilon_2(\omega)}{\varepsilon_1^2(\omega) + \varepsilon_2^2(\omega)} \quad (8)$$

Dielectric function is shown in Fig 5. It can be found that static dielectric constant  $\epsilon_1(0)$  of intrinsic  $\text{PbTiO}_3$  is 6.57 at 0eV, which is well in good agreement with the previous theoretical results (6.45 and 6.59) [35, 49]. With the increase of photon energy,  $\epsilon_1$  starts to increase and reaches the maximum value of 10.05 at 3.11eV. After doping with B (N) atom, static dielectric constant becomes larger, and the maximum value of  $\epsilon_{1B}(0)$  ( $\epsilon_{1N}(0)$ ) is 12.55 (13.03), expounding that the polarization ability of the doping system is stronger, and the binding ability of the charge is stronger. Imaginary part  $\epsilon_2$  of dielectric function has five prominent peaks, which are labeled as A (5.81eV), B (13.94eV), C (22.08 eV), D (28.25 eV) and E (36.54eV). The peak value of dielectric function is closely related to band structure of the material and electronic excitation [50]. The main peak A is much stronger than the others, peak A originated from the transition of electrons from occupied O-2p VB states to unoccupied Ti-3d CB states. In order to confirm the authenticity of our calculated optical properties, we compare our results with the results of Taib *et al.* [49]. There are also five main peaks, the first four main peaks are A (6.21 eV), B (13.4 eV), C (21.28) and D (27.85 eV). In contrast, our main peak A is redshifted by 0.4eV, and main peaks B, C and D are blue-shifted by 0.54eV, 0.8eV and 0.4eV, respectively. In the low energy region, the value of  $\epsilon_2$  is almost zero. However,  $\epsilon_2$  of B- and N-doped  $\text{PbTiO}_3$  both have a peak in the low energy region. From the analysis of energy band structure and DOS spectrum, it is known that this is due to the formation of B-2p impurity states and N-2p impurity states.

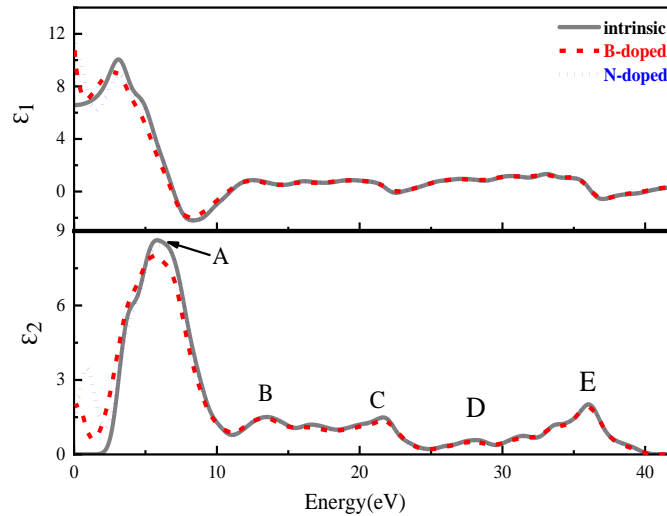


Fig. 5. Calculated dielectric function of intrinsic, B- and N-doped  $\text{PbTiO}_3$ .

The calculated absorption coefficient in the range of 0 to 1200 nm is depicted in Fig. 6. When the wavelength reaches 155nm, absorption coefficient of intrinsic  $\text{PbTiO}_3$  reaches the peak value of  $252409 \text{ cm}^{-1}$ . In contrast, the peak of B-doped  $\text{PbTiO}_3$  is almost the same as that of intrinsic  $\text{PbTiO}_3$ , and the peak of N-doped  $\text{PbTiO}_3$  is even smaller than that of intrinsic  $\text{PbTiO}_3$ . This imply that B- and N-doped systems cannot effectively improve the light absorption performance in the UV region with a wavelength of less than 250 nm. It is worth noting that absorption coefficient of intrinsic  $\text{PbTiO}_3$  at wavelengths greater than 569nm is almost zero, which means that intrinsic  $\text{PbTiO}_3$  is always transparent at wavelengths greater than 569nm, because the range of this part of photon is just within the forbidden band. Fortunately, compared with intrinsic  $\text{PbTiO}_3$ , B- and N-doped  $\text{PbTiO}_3$  systems have higher light absorption coefficients in the visible

and near-infrared regions. They exhibit excellent optical properties, which emphasizes that doped system can make better use of visible light. It is of great significance for improving light absorption performance of visible light and near-infrared light.

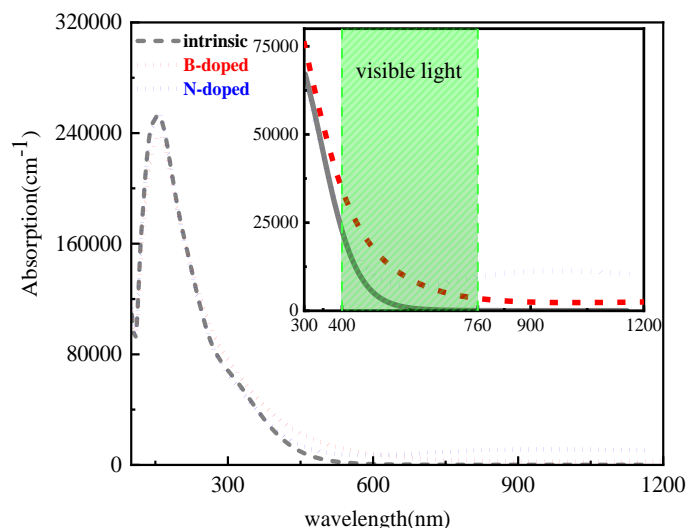


Fig. 6. Variation of the adsorption coefficient versus photon energy of intrinsic, B- and N-doped  $\text{PbTiO}_3$ .

Refractive index in the range of energy (0 to 42 eV) and wavelength (0 to 1200nm) are shown in Fig 7. Static refractive index  $n(0)$  of intrinsic  $\text{PbTiO}_3$ , B- and N-doped  $\text{PbTiO}_3$  are 2.56, 3.55 and 3.61, respectively. It can be seen from equation (2) that refractive index corresponds to real part of dielectric function. Compared with intrinsic  $\text{PbTiO}_3$ , static refractive index of B- and N-doped  $\text{PbTiO}_3$  are larger, and refractive index change trend of intrinsic, B- and N-doped  $\text{PbTiO}_3$  are almost the same as the change trend of real part. We compare our results with some previous experimental and theoretical data as presented in Table 3. Among them, our result is 2.9% larger than single crystal [51] and thin film [52] experimental results, and it is in good agreement with other theoretical value [35, 53].

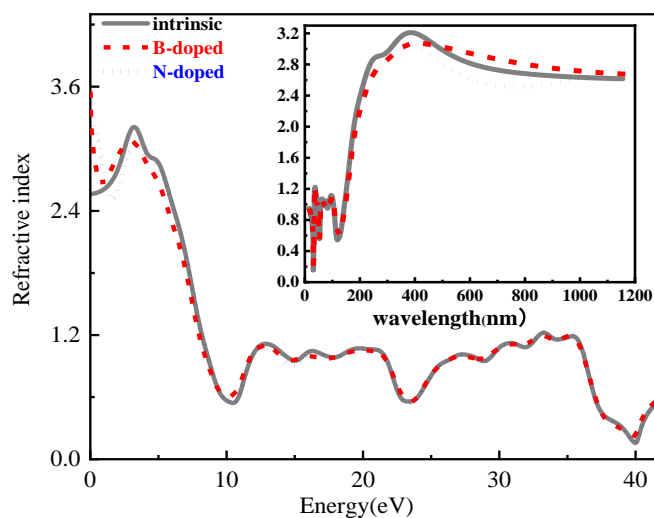
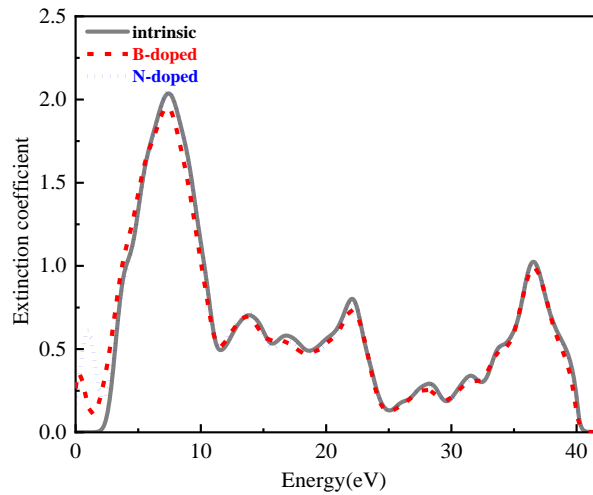


Fig. 7. The refractive index of intrinsic, B- and N-doped  $\text{PbTiO}_3$ .

Table 3. Some previous experimental and theoretical data of refractive index.

Methods		Refractive index ( $n$ )
Experimental	Single crystal at 632.8nm [51]	2.7
	Thin film at 633nm [52]	
Theory	GGA-PBE (this work) at 628.8nm	2.78
	FP-LAPW (GGA96) at 0 eV [35]	2.56
GGA-PBE (this work) at 0 eV		2.56
FP-LAPW (GGA96) at 830nm [35]		2.61
GGA-PBE (this work) at 837nm		2.67
Point-dipole approach at 1152 nm [53]		2.56
GGA-PBE (this work) at 1156nm		2.61

Extinction coefficient is plotted in Fig.8. Extinction coefficient  $k(\omega)$  of intrinsic  $\text{PbTiO}_3$  whose frequency is less than 1.03 eV range is zero, which is consistent with our calculation of absorption edge (1.03 eV) of absorption function. By analyzing DOS spectrum, there are several electrons distributed near 0 eV, which causes absorption edge to be smaller than our calculated band gaps (2.02eV). In the low energy range, extinction coefficient of B-doped (N-doped)  $\text{PbTiO}_3$  has an additional peak, which comes from the electronic transition between O-2p, B-2p(N-2p) and Ti-3d states.

Fig. 8. Calculated extinction coefficient of intrinsic, B- and N-doped  $\text{PbTiO}_3$ .

Energy loss function, which is energy loss of electrons passing through a uniform dielectric solid material [54], is presented in Fig.9. Intrinsic, B- and N-doped  $\text{PbTiO}_3$  all have three peaks, and energy loss is the largest when it is about 41.1eV, they correspond to the energy at the edge of plasma. The other two peaks are around 11.0 eV and 23.6 eV. In the range of visible light (1.64 to 3.19eV), energy loss of B- and N-doped  $\text{PbTiO}_3$  is larger than that of intrinsic  $\text{PbTiO}_3$ , but energy loss of the three systems is very small.

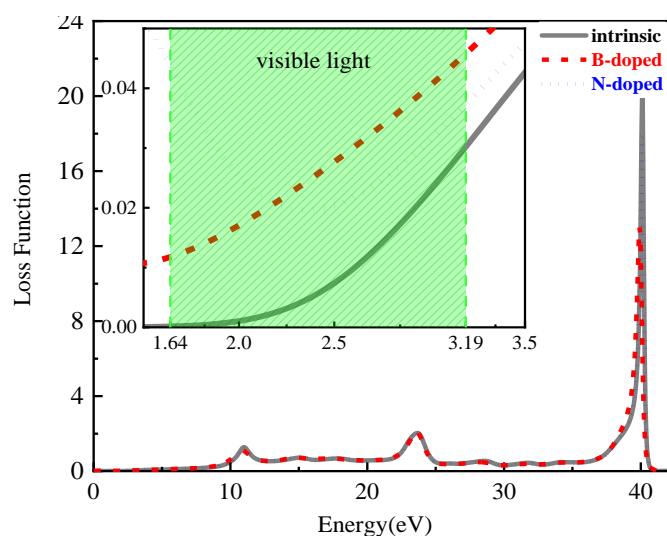


Fig. 9. Loss function of intrinsic, B- and N-doped  $\text{PbTiO}_3$  as a function of energy.

#### 4. Conclusions

In summary, the lattice structure, electron and optical properties of intrinsic, B- and N-doped  $\text{PbTiO}_3$  are studied in detail via first-principles. After doping B (N) atom, the structural stability of the system is lowered, but they are still thermodynamically stable. Electron density difference emphasizes that Ti-O atoms form strong covalent bonds. Pb-O bond is not a pure ionic bond, and there are certain covalent components. Comparison with intrinsic  $\text{PbTiO}_3$ , the bond length increases and bond population decreases after doping with B (N) atom.

The B-2p (N-2p) impurity states near Fermi level increase the probability of the electron transition from CB to VB, leading to significantly narrower bandwidth for B-doped (N-doped)  $\text{PbTiO}_3$  than for intrinsic  $\text{PbTiO}_3$ . Imaginary part of dielectric function has the largest peak at the photon energy of 5.81 eV, and the peak originates from the transition of electrons from the occupied O-2p VB states to the unoccupied Ti-3d CB states. The static refractive index of B- and N-doped  $\text{PbTiO}_3$  both are larger than that of  $\text{PbTiO}_3$ . In addition, absorption coefficient and the energy loss indicate that B- and N-doping may improve the optical properties of  $\text{PbTiO}_3$ .

#### Acknowledgements

This work is supported by Guangxi Natural Science Foundation, China (No. 2019GXNSFBA245092, 2019GXNSFGA245006), the Science and Foundation of Guilin University of Technology (No. GUTQDJJ2019116) and the National Natural Science Foundation of China (Nos. 52062010).

## References

- [1] P. J. Niu, J. L. Yan, C. Y. Xu, *Comput. Mater. Sci.* 98, 10 (2015); <https://doi.org/10.1016/j.commatsci.2014.10.057>
- [2] H. Hashima, S. Nakajima, Y. Suzuki, S. Ogawa, *Thin Solid Films* 281-282, 463 (1996); [https://doi.org/10.1016/0040-6090\(96\)08676-2](https://doi.org/10.1016/0040-6090(96)08676-2)
- [3] M. Okuyama, Y. Hamakawa, *Ferroelectrics* 63(1), 243 (2011); <https://doi.org/10.1080/00150198508221406>
- [4] T. W. Kim, D. U. Lee, Y. S. Yoon, C. H. Wang, S. S. Yom, S. J. Lee, C. O. Kim, *Solid State Commun.* 96(2), 95 (1995); [https://doi.org/10.1016/0038-1098\(95\)00270-7](https://doi.org/10.1016/0038-1098(95)00270-7)
- [5] P. Erhart, K. Albe, *Comput. Mater. Sci.* 103, 224 (2015); <https://doi.org/10.1016/j.commatsci.2015.02.029>
- [6] M. Okuyama, Y. Togami, Y. Hamakawa, *Appl. Surf. Sci.* 33, 625 (1988); [https://doi.org/10.1016/0169-4332\(88\)90361-3](https://doi.org/10.1016/0169-4332(88)90361-3)
- [7] H. Lv, H. Gao, Y. Yang, L. Liu, *Appl. Catal. A: Gen.* 404 (1-2), 54 (2011).
- [8] L. Q. Chen, Y. Zhao, *Prog. Mater. Sci.*, 124, 100868 (2022); <https://doi.org/10.1016/j.pmatsci.2021.100868>
- [9] R. J. Nelmes, W. F. Kuhs, *Solid State Commun.* 54(8), 721 (1985); [https://doi.org/10.1016/0038-1098\(85\)90595-2](https://doi.org/10.1016/0038-1098(85)90595-2)
- [10] G. Shirane, R. Pepinsky, B. C. Frazer, *Acta Crystallogr.* 9(4), 131 (1956); <https://doi.org/10.1107/S0365110X56000309>
- [11] F. F. Ge, W. D. Wu, X. M. Wang, H. P. Wang, Y. Dai, H. B. Wang, J. Shen, *Physica B* 404(20), 3814 (2009); <https://doi.org/10.1016/j.physb.2009.06.150>
- [12] N. V. Minh, L. M. Oanh, P. Van. Doan, P. V. Hai, L. H. Hoang, *Ceram. Int.* 37(8), 3785 (2011); <https://doi.org/10.1016/j.ceramint.2011.06.017>
- [13] J. R. Zhang, Y. C. Zhang, C. J. Lu, W. N. Ye, J. Su, *J. Mater. Sci. Mater. Electron.* 25(2), 653 (2014).
- [14] Z. Yao, H. Liu, M. Cao, H. Hao, Z. Yu, *Mater. Res. Bull.* 46(8), 1257 (2011); <https://doi.org/10.1016/j.materresbull.2011.03.034>
- [15] N. Sahu, S. Panigrahi, M. Kar, *Adv. Powder Technol.* 22(6), 689 (2011); <https://doi.org/10.1016/j.appt.2010.10.007>
- [16] A. Stashans, C. Zambrano, A. Sanchez, L. M. Procel, *Int. J. Quantum Chem* 87(3), 145 (2002); <https://doi.org/10.1002/qua.10034>
- [17] J. Wu, H. Shi, T. Zhao, Y. Yu, S. Dong, *Adv. Funct. Mater.* 26(39), 7186 (2016); <https://doi.org/10.1002/adfm.201602645>
- [18] S. Piskunov, E. Heifets, R. I. Eglitis, G. Borstel, *Comput. Mater. Sci.* 29(2), 165 (2004); <https://doi.org/10.1016/j.commatsci.2003.08.036>
- [19] E. R. Leite, L. P. S. Santos, N. L. V. Carreño, E. Longo, C. A. Paskocimas, J. A. Varela, F. L. Jr, C. E. M. Campos, P. S. Pizani, *Appl. Phys. Lett.* 78(15), 2148 (2001); <https://doi.org/10.1063/1.1362200>
- [20] H. O. Yadav, *Ceram. Int.* 30(7), 1493 (2004); <https://doi.org/10.1016/j.ceramint.2003.12.133>
- [21] H. X. Zhu, X. H. Wang, D. F. Zhou, H. Jiang, X. M. Liu, *Phys. Lett. A* 384(26), 126637

- (2020); <https://doi.org/10.1016/j.physleta.2020.126637>
- [22] L. M. Oanh, D. B. Do, N. D. Phu, N. T. P. Mai, N. V. Minh, IEEE Trans. Magn. 50(6), 1 (2014); <https://doi.org/10.1109/TMAG.2014.2376731>
- [23] R. Abirami, T. S. Senthil, S. Kalpana, L. Kungumadevi, M. Kang, Mater. Lett. 279, 128507 (2020); <https://doi.org/10.1016/j.matlet.2020.128507>
- [24] H. Lemziouka, L. E. H. Omari, R. Moubah, A. Boutahar, S. Bahhar, M. H. Abid, H. Lassri, Materials Today: Proceedings 37(17), 3940 (2021); <https://doi.org/10.1016/j.matpr.2020.09.094>
- [25] P. J. Niu, J. L. Yan, D. Meng, J. Semicond. 36(4), 30 (2015); <https://doi.org/10.1088/1674-4926/36/4/043004>
- [26] J. P. Perdew, Phys. Rev. B: Condens. Matter 33(12), 8822 (1986); <https://doi.org/10.1103/PhysRevB.33.8822>
- [27] M. D. Segall, P. J. D. Lindan, M. J. Probert, C. J. Pickard, P. J. Hasnip, S. J. Clark, M. C. Payne, J. Phys.: Condens. Matter 14(11), 2717 (2002); <https://doi.org/10.1088/0953-8984/14/11/301>
- [28] K. Laasonen, A. Pasquarello, R. Car, C. Lee, Vanderbilt, D. Phys. Rev. B: Condens. Matter 47(16), 10142 (1993); <https://doi.org/10.1103/PhysRevB.47.10142>
- [29] J. P. Perdew, K. Burke, M. Ernzerhof, Phys Rev Lett 77(18), 3865 (1996); <https://doi.org/10.1103/PhysRevLett.77.3865>
- [30] T. Shimada, T. Ueda, J. Wang, T. Kitamura, Phys. Rev. B 87(17), 174111 (2013); <https://doi.org/10.1103/PhysRevB.87.174111>
- [31] L. Wang, P. Yuan, F. Wang, E. Liang, Q. Sun, Z. Guo, Y. Jia, Mater. Res. Bull., 49, 509 (2014); <https://doi.org/10.1016/j.materresbull.2013.08.075>
- [32] Y. Zhang, J. Sun, J. P. Perdew, X. Wu, Phys. Rev. B 96(3), 035143 (2017); <https://doi.org/10.1103/PhysRevB.96.035143>
- [33] X. Liu, J. Fu, G. Chen, RSC Adv. 10(29), 17317 (2020); <https://doi.org/10.1039/C9RA10735E>
- [34] Y. Pan, W. M. Guan, K. H. Zhang, Physica B 427, 17 (2013); <https://doi.org/10.1016/j.physb.2013.05.039>
- [35] S. M. Hosseini, T. Movlaroooy, A. Kompany, Eur. Phys. J. B 46(4), 463 (2005); <https://doi.org/10.1140/epjb/e2005-00275-3>
- [36] S. M. Hosseini, T. Movlaroooy, A. Kompany, Physica B 391(2), 316 (2007); <https://doi.org/10.1016/j.physb.2006.10.013>
- [37] J. Sun, X. F. Zhou, Y. X. Fan, J. Chen, H. T. Wang, X. Guo, J. He, Y. Tian, Phys. Rev. B 73(4), 45108 (2006).
- [38] M. D. Segall, R. Shah, C. J. Pickard, M. C. Payne, Phys. Rev. B: Condens. Matter 54(23), 16317 (1996); <https://doi.org/10.1103/PhysRevB.54.16317>
- [39] Y. Kuroiwa, S. Aoyagi, A. Sawada, J. Harada, M. Sakata, Phys. Rev. Lett 87(21), 217601 (2001); <https://doi.org/10.1103/PhysRevLett.87.217601>
- [40] R. E. Cohen, Nature 359, 136 (1992); <https://doi.org/10.1038/358136a0>
- [41] V. Železný, D. Chvostová, D. Šimek, F. Máca, J. Mašek, N. Setter, Y. H. Huang, J. Phys.: Condens. Matter 28(2), 025501 (2016); <https://doi.org/10.1088/0953-8984/28/2/025501>
- [42] W. Setyawan, S. Curtarolo, Comput. Mater. Sci. 49(2), 299 (2010);

<https://doi.org/10.1016/j.commatsci.2010.05.010>

- [43] W. Y. Ching, Y. N. Xu, K. W. Wong, *Phys. Rev. B: Condens. Matter* 40(11), 7684 (1989); <https://doi.org/10.1103/PhysRevB.40.7684>
- [44] Z. Li, J. Li, J. Lei, M. Xiong, S. Zhang, *Vacuum* 186(45), 110062 (2021); <https://doi.org/10.1016/j.vacuum.2021.110062>
- [45] J. Park, Y. N. Wu, W. A. Saidi, B. Chorpening, Y. Duan, *Phys. Chem. Chem. Phys.* 22(46), 27163 (2020); <https://doi.org/10.1039/D0CP05445C>
- [46] H. Wang, N. Lin, R. Xu, Y. Yu, X. Zhao, *Chem. Phys.* 539, 110972 (2020); <https://doi.org/10.1016/j.chemphys.2020.110972>
- [47] A. E. Yousfi, H. Bouda, A. G. E. Hachimi, M. A. ArshAd, A. E. Kenz, A. Benyoussef, *Opt Quantum Electron* 53(2), 1 (2021); <https://doi.org/10.1007/s11082-021-02735-z>
- [48] Z. Q. Jiang, G. Yao, X. Y. An, Y. J. Fu, L. H. Cao, W. D. Wu, X. M. Wang, *Chinese Phys. B* 23(5), 057104 (2014); <https://doi.org/10.1088/1674-1056/23/5/057104>
- [49] M. F. M. Taib, M. K. Yaakob, F. W. Badrudin, M. S. A. Rasiman, M. Z. A. Yahya, *Integr. Ferroelectr.* 155(1), 23 (2014); <https://doi.org/10.1080/10584587.2014.905105>
- [50] Y. Duan, P. Ohodnicki, B. Chorpening, G. Hackett, *J. Solid State Chem.* 256(1), 239 (2017); <https://doi.org/10.1016/j.jssc.2017.09.016>
- [51] S. Singh, J. P. Remeika, J. R. Potopowicz, *Appl. Phys. Lett.* 20(3), 135 (1972); <https://doi.org/10.1063/1.1654078>
- [52] M. Okuyama, T. Usuki, Y. Hamakawa, T. Nakagawa, *Appl. Phys.* 21(4), (1980), 339; <https://doi.org/10.1007/BF00895925>
- [53] D. Khatib, K. Bammou, F. Bensamka, L. Hafid, *Ferroelectrics Lett.* 25(5-6), 117 (1999); <https://doi.org/10.1080/07315179908204641>
- [54] B. Luo, X. Wang, E. Tian, G. Li, L. Li, *J. Mater. Chem. C* 3(33), 8625 (2015); <https://doi.org/10.1039/C5TC01622C>